

# Surface wave imaging of the weakly extended Malawi Rift from ambient-noise and telesismic Rayleigh waves from onshore and lake-bottom seismometers

N.J. Accardo,<sup>1</sup> J.B. Gaherty,<sup>1</sup> D.J. Shillington,<sup>1</sup> C.J. Ebinger,<sup>2</sup> A.A. Nyblade,<sup>3</sup> G.J. Mbogoni,<sup>4</sup> P.R.N. Chindandali,<sup>5</sup> R.W. Ferdinand,<sup>6</sup> G.D. Mulibo,<sup>6</sup> G. Kamihanda,<sup>4</sup> D. Keir,<sup>7,8</sup> C. Scholz,<sup>9</sup> K. Selway,<sup>10</sup> J.P. O'Donnell,<sup>11</sup> G. Tepp,<sup>12</sup> R. Gallacher,<sup>7</sup> K. Mtelela,<sup>6</sup> J. Salima<sup>5</sup> and A. Mruma<sup>4</sup>

<sup>1</sup>Lamont-Doherty Earth Observatory of Columbia University, Palisades, NY 10964, USA. E-mail: [accardo@ldeo.columbia.edu](mailto:accardo@ldeo.columbia.edu)

<sup>2</sup>Department of Earth and Environmental Sciences, Tulane University, New Orleans, LA 70118, USA

<sup>3</sup>Department of Geosciences, The Pennsylvania State University, State College, PA 16802, USA

<sup>4</sup>Geological Survey of Tanzania, Dodoma, Tanzania

<sup>5</sup>Geological Survey Department of Malawi, Zomba, Malawi

<sup>6</sup>Department of Geology, University of Dar es Salaam, Dar es Salaam, Tanzania

<sup>7</sup>National Oceanography Centre Southampton, University of Southampton, Southampton SO17 1BJ, United Kingdom

<sup>8</sup>Dipartimento di Scienze della Terra, Università degli Studi di Firenze, Florence 50121, Italy

<sup>9</sup>Department of Earth Sciences, Syracuse University, New York, NY 13210, USA

<sup>10</sup>Department of Earth and Planetary Sciences, Macquarie University, NSW 2109, Australia

<sup>11</sup>School of Earth and Environment, University of Leeds, Leeds, LS2 9JT, United Kingdom

<sup>12</sup>Alaska Volcano Observatory, U.S. Geological Survey, Anchorage, AK 99775, USA

Accepted 2017 March 28. Received 2017 March 13; in original form 2016 October 12

## SUMMARY

Located at the southernmost sector of the Western Branch of the East African Rift System, the Malawi Rift exemplifies an active, magma-poor, weakly extended continental rift. To investigate the controls on rifting, we image crustal and uppermost mantle structure beneath the region using ambient-noise and telesismic Rayleigh-wave phase velocities between 9 and 100 s period. Our study includes six lake-bottom seismometers located in Lake Malawi (Nyasa), the first time seismometers have been deployed in any of the African rift lakes. Noise levels in the lake are lower than that of shallow oceanic environments and allow successful application of compliance corrections and instrument orientation determination. Resulting phase-velocity maps reveal slow velocities primarily confined to Lake Malawi at short periods ( $T \leq 12$  s), indicating thick sediments in the border-fault bounded rift basin. The slowest velocities occur within the Central Basin where Malawi Rift sedimentary strata may overlie older (Permo-Triassic) Karoo group sediments. At longer periods ( $T > 25$  s), a prominent low-velocity anomaly exists beneath the Rungwe Volcanic Province at the northern terminus of the rift basin. Estimates of phase-velocity sensitivity indicates these low velocities occur within the lithospheric mantle and potentially uppermost asthenosphere, suggesting that mantle processes may control the association of volcanic centres and the localization of magmatism. Beneath the main portion of the Malawi Rift, a modest reduction in velocity is also observed at periods sensitive to the crust and upper mantle, but these velocities are much higher than those observed beneath Rungwe.

**Key words:** Seismic instruments; Seismic noise; Seismic tomography; Surface waves and free oscillations; Continental tectonics: extensional.

## 1 INTRODUCTION

A fundamental question in continental dynamics asks how strong lithospheric plates rupture, given the modest magnitude of available tectonic forces (i.e. slab pull and ridge push; e.g. Forsyth & Uyeda

1975; Bott 1991). Lithospheric strain localization and strength reduction during early-stage rifting is achieved in models that include weakening mechanisms like magmatic intrusions to enable continental rupture (Buck 2004, 2006). In the past two decades, field, laboratory and modeling studies of mature continental rift systems

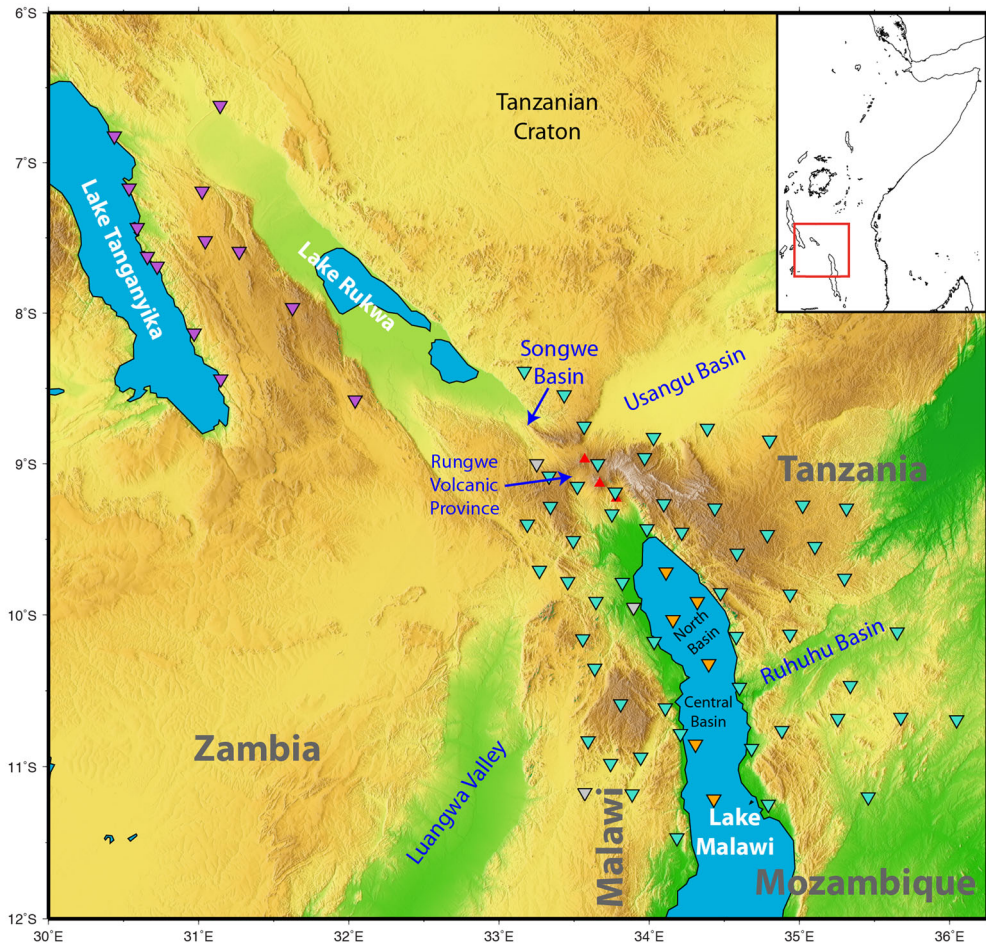


**Figure 1.** Map of the Malawi-Rukwa region with major tectonic features labeled. Inset map shows location of the study region. Upside-down triangles indicate the locations of the four seismic arrays used in this study: purple—TANGA, turquoise—SEGMeNT onshore, orange—SEGMeNT offshore, grey—Africa Array, Malawi Seismic Network. Red triangles represent the locations of the three volcanoes of the Rungwe Volcanic Province (RVP).

increasingly point to the influential role of melt products on the evolution of continental rifting (e.g. Ebinger & Casey 2001; Corti *et al.* 2003; Dugda *et al.* 2005; Kendall *et al.* 2005; Buck 2006; Bastow & Keir 2011; Armitage *et al.* 2015). However, many ancient and active rift systems display evidence of volumetrically limited magmatic activity, for example, the Western Branch of the East African Rift System (EARS; Furman 2007) and the Newfoundland-Iberia rifted margins (e.g. Whitmarsh *et al.* 2000; Van Avendonk *et al.* 2009). To shed light on extensional processes in an immature rift, including the controls of magmatism on extension, the SEGMeNT (Study of Extension and maGmatism in Malawi aNd Tanzania) experiment acquired a suite of data sets including GPS, active- and passive-source seismic, geochemical and magnetotelluric data across the Malawi Rift (Shillington *et al.* 2016), where volcanism is restricted to the northern axial termination. Data from the Southern Lake Tanganyika Experiment (TANGA) are used to help constrain structure beyond the northern limits of the Rungwe Volcanic Province (RVP). Our study presents the first locally constrained seismic tomographic maps of surface wave phase velocity of the Malawi Rift with the aim of illuminating crust and upper-mantle structure beneath the region.

## 2 TECTONIC SETTING

The Malawi Rift, located in the southernmost sector of the EARS, is a seismically active, magma-poor, weakly extended continental

rift. The Malawi Rift extends over 800 km from the RVP in the north to the Urema Graben (Mozambique) in the south (Fig. 1). Lake Malawi (Nyasa) covers approximately 550 km of the rift axis, and is a type example of a narrow and deep East African rift lake. The Malawi Rift shares many similarities with other Western Branch rift basins, including strong lithosphere with deep seismicity (Ebinger *et al.* 1989; Jackson & Blenkinsop 1993; Craig *et al.* 2011; Fagereng 2013), limited surface magmatism (Furman 2007) and asymmetric border-fault-bounded half grabens with polarities that vary along the rift (Crossley & Crow 1980; Rosendahl *et al.* 1992).

The border-fault-bounded half grabens partition Lake Malawi into three basins (North, Central and South) linked via complex transfer zones (Scholz *et al.* 1989). These basins developed within Proterozoic mobile belts, with the eastern boundary of Lake Malawi abutting the juncture between the Irumide Belt to the west and the Mozambique and Ubendian belts to the north and east (e.g. Chorowicz 2005; Begg *et al.* 2009). Fault-bounded depressions to the west and east of the Central Basin (Luangwa Valley and Ruhuhu Basin, respectively) represent Karoo rift basins (e.g. Catuneanu *et al.* 2005) formed in the Late Carboniferous associated with early Gondwana breakup (Wopfner 1994, 2002). Little stretching is thought to have occurred in the Malawi Rift with crustal stretching estimates from flexural models of basin and flank morphology and fault reconstructions suggesting <20 per cent (Ebinger *et al.*

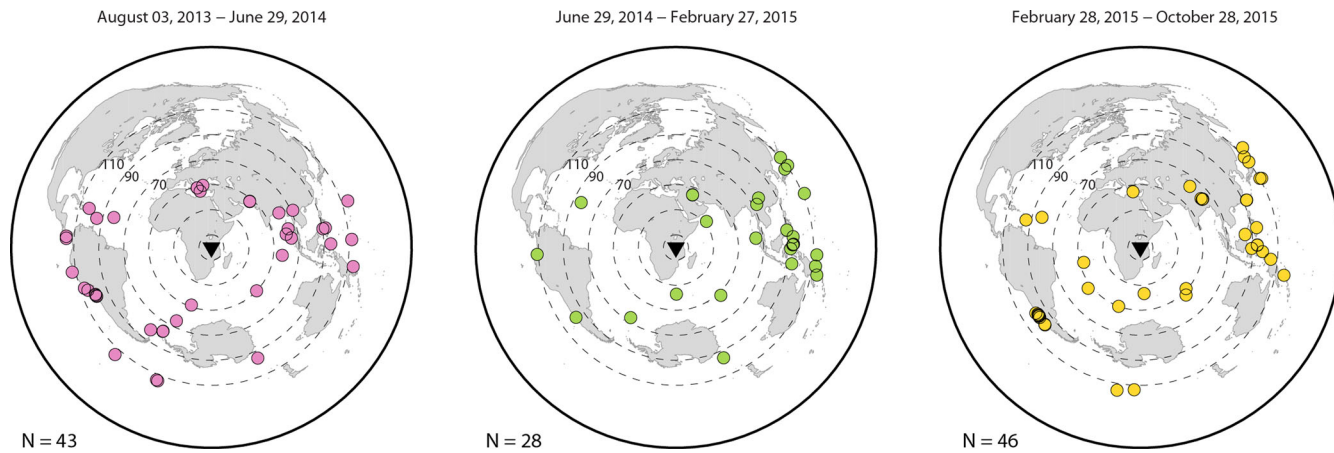


**Figure 2.** Event distribution used in this study. The distribution of events is shown for the three time periods of interest for the SEGMeNT study. 2013 August 3–2014 June 29: deployment of initial 13 instruments in the Rungwe/Tukuyu area. 2014 June 29–2015 February 27: addition of 42 broad-band stations in Malawi and Tanzania. 2015 February 28–October 28, 2015: addition of six broad-band LBS in Lake Malawi. The entire array was pulled out by 2015 October 28. Locations of events are shown by the circles, and the study region is shown by the triangle. All events were above a magnitude ( $M_w$ ) 6.0 and occurred at depths <50 km. The number of events for each time period are shown in the bottom left of each panel.

1987). Furthermore, data from a single GPS within the Malawi Rift estimate a plate-opening velocity of *ca.* 1 mm yr<sup>-1</sup> (Saria *et al.* 2014).

The RVP at the northern end of the Malawi Rift is one of four volcanic centres within the Western Branch of the EARS (Furman 2007) and represents the southernmost expression of volcanism in the entire rift system. The RVP sits within the complex accommodation zone between the Malawi, Rukwa and the apparently inactive Usangu rifts. Three volcanoes within the RVP (from north to south: Ngozi, Rungwe and Kyejo, Fig. 1) have erupted in the past 10 Ka (Ebinger *et al.* 1989; Fontijn *et al.* 2010a,b, 2012). Debate continues concerning the relative timing of the onset of rifting within the Rukwa-Malawi rift zones, owing to the lack of deep drill data. Magmatism in the RVP may have commenced as early as 25 Ma (Roberts *et al.* 2012), much earlier than the onset of faulting estimated at 8.6 Ma (Ebinger *et al.* 1993) along the northern basin bounding fault (Ebinger *et al.* 1989).

Previous seismic investigations of the Malawi Rift have been limited to the extremes of the spatial spectrum: basin-scale investigations of Lake Malawi's shallow stratigraphy (e.g. Scholz & Rosendahl 1988; Specht & Rosendahl 1989), and regional to continental studies of the entire EARS (e.g. Weeraratne *et al.* 2003; Pasyanos & Nyblade 2007; Fishwick 2010). Recent regional-scale studies using surface and body waves image a circular low-velocity region centred on the RVP within the uppermost mantle, which weakens and becomes more diffuse at greater depths (~140 km; Adams *et al.* 2012; Mulibbo & Nyblade 2013; O'Donnell *et al.* 2013). The Pn/Sn study of O'Donnell *et al.* (2016) attribute the RVP low-velocity anomaly to pervasive thermal alteration of the uppermost mantle and potentially the presence of melt. These larger scale studies lack the resolution to delineate the detailed structure of the low-velocity region and the degree to which it extends south into the Malawi rift basin, and to characterize the crustal and upper-mantle manifestation of the rift. The combined SEGMeNT and TANGA experiments include a unique broad-band seismic array that utilizes onshore and offshore instrumentation to span the RVP and Lake Malawi. Rayleigh waves traversing the array provide unsurpassed sampling of crustal and upper-mantle structure across the Malawi Rift.

### 3 DATA AND METHODS

We collected Rayleigh waves derived from both ambient-noise and teleseismic earthquakes recorded on the onshore/offshore SEGMeNT and onshore TANGA stations (Fig. 1). Combined, these two temporary networks provide 72 intermediate-period and broad-band seismometers with a total array aperture of ~400 km.

The utilization of both ambient-noise and earthquake-generated Rayleigh waves to constrain Earth structure is increasingly employed due to the complementary nature of the two data sets (e.g. Jin *et al.* 2015). Ambient-noise surface waves allow access to shorter periods where regional and teleseismic surface waves become attenuated and scattered, while earthquake observations provide considerably higher signal-to-noise ratio at longer periods (~>25 s) where ambient-noise observations commonly suffer from decreased quality.

#### 3.1 Earthquake processing: determination of dynamic and structural phase velocity

We measured Rayleigh-wave phase velocities between 20 and 100 s from regional and teleseismic records. We initially selected all events (total of 141) with  $M_w$  greater than 6.0 between epicentral distances of 5° and 115° and depths <50 km. All events selected were visually inspected for quality and were required to have been recorded on a minimum of seven stations. This has resulted in the inclusion of a total of 117 earthquakes that are well distributed in azimuth in the final phase-velocity images (Fig. 2). An example of a high-quality event can be seen in Fig. 3(a).

We utilize the multichannel cross-correlation technique of Jin & Gaherty (2015) that leverages the coherence between traces from nearby stations to determine Rayleigh-wave phase velocity. This method recovers frequency-dependent phase and amplitude information via the narrow-band filtering of the broad-band (10–150 s) cross-correlation function (CCF) between the vertical-component seismic trace from a given station and time-windowed traces from all stations where interstation distances were between 20 and 200 km. For this study, the filters were constructed as zero-phase Gaussian filters centred at 20, 25, 32, 40, 50, 60, 80 and 100 s and a bandwidth of 10 per cent of the centre frequency. The phase and amplitude

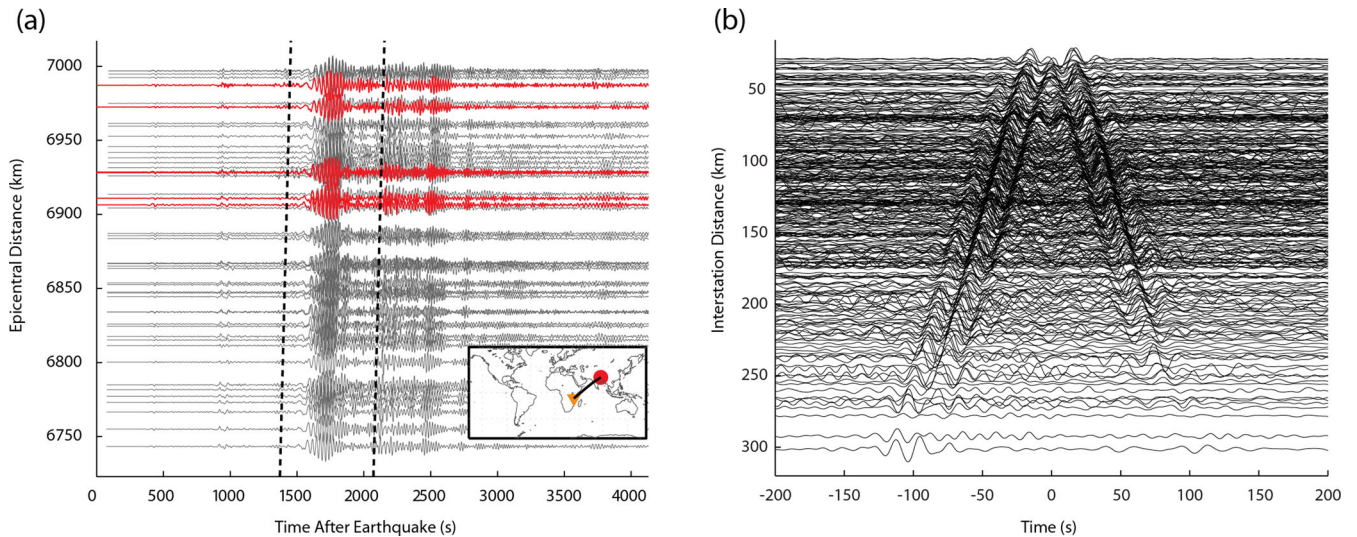


**Figure 3.** Examples of (a) teleseismic and (b) ambient-noise Rayleigh waves used in this study. (a) Record section from the  $M_w$  7.8 event on 2015 April 25. Location of the event (red circle) and seismic array (orange triangle) are shown in the inset. Grey: onshore stations and red: lake-bottom seismometers. Data have been filtered from 10 to 100 s. (b) Ambient noise cross-correlation functions in the time domain for all stations pairs that include a lake-bottom seismometer. Data have been filtered from 8 to 25 s.

information is determined by fitting the narrow-band filtered CCF with a Gaussian wavelet characterized by five parameters: the positive scale factor  $A$ , the centre frequency  $\omega_s$ , the half-bandwidth  $\sigma_s$ , the group delay  $t_g$  and the phase delay  $t_p$ .

Assuming that the broad-band seismograms recorded at nearby stations are similar, the network of multichannel phase delays ( $t_p$ ) provide highly precise, robust constraints on the spatial variation of phase speed. To remove the influence of poor-quality seismic traces, we estimate the coherence between waveforms from nearby stations at a series of frequencies. For this study, we include only those measurements with coherence  $>0.5$ . We further test for outlying phase observations (potentially resulting from poor signal quality or undetected cycle-skipping) by comparing each measurement to that predicted from the average apparent phase velocity for a given frequency across the entire network. We discard individual phase delay measurements ( $\sim 2$  per cent) with outlying values that would require greater than 20 per cent perturbation to the predicted determined reference value. Additionally, we minimize the likelihood of erroneous phase measurements arising from cycle-skipping by limiting available station pairs to those with interstation distances  $<200$  km. This length scale is less than three times the wavelength of the shortest period teleseismic Rayleigh wave (20 s).

At each frequency, we invert the network of phase delays for spatial variations in dynamic phase velocity via the eikonal equation (Lin *et al.* 2009). We tested the influence of smoothness choices on the inversion for individual event results and also on the final stacked solutions. To stabilize the inversion for individual event phase-velocity maps, we applied a smoothness constraint that minimizes the second derivative of the slowness vector calculated from derived maps of phase delay. The weight of the smoothness constraint was chosen based on the frequency of interest and after testing the influence of smoothness on data fit. We applied the same weighting parameters to all events. After stacking all individual event results, we smooth the resulting phase-velocity map based on the wavelength of the frequency of interest. We set the length of smoothing to be 25 per cent of the average wavelength at each frequency.

We next correct for the influence of focusing and defocusing of the wavefield via Helmholtz tomography (Lin & Ritzwoller 2011), producing maps of structural phase velocity at each frequency for

each event. After applying strict quality control standards to each individual event result (discussed below), final event solutions are stacked to obtain robust structural phase velocity estimates at all periods at every grid point within the array. Additional information concerning the determination of structural phase velocity (i.e. standard deviation of the resulting phase-velocity maps and the total number of crossing interstation paths) can be found in the Supporting Information.

The Helmholtz equation is given by

$$\frac{1}{c(\vec{r})^2} = \frac{1}{c'(\vec{r})^2} - \frac{\nabla^2 A(\vec{r})}{A(\vec{r}) \omega^2} \quad (1)$$

where  $c(\vec{r})$  is the structural phase velocity,  $c'(\vec{r})$  is dynamic phase velocity,  $A(\vec{r})$  is the amplitude field,  $\omega$  is angular frequency and  $\vec{r}$  is the path connecting two stations. Henceforth, we call this amplitude-correction term applied to the dynamic phase velocity as the ‘correction term’. Jin & Gaherty (2015) discuss several complexities inherent in the construction of this correction term including ensuring smoothness in the amplitude field, smoothness in the resulting Laplacian of the amplitude field and avoiding the influence of site-specific amplification effects. In the ideal case, all stations in an array would have a site amplification term of unity. However, variations in local geology or instrument and/or installation conditions can cause amplification terms to deviate away from unity causing the resulting amplitude and correction terms to be biased.

To minimize such biases, we first correct event-specific amplitude fields with estimated station amplification terms prior to applying Helmholtz tomography. We calculate the median normalized amplitude value for a given station across all events, where normalized amplitude is calculated as a station’s amplitude measurement normalized by the median of all amplitude measurements for the network for that event. Fig. 4 shows an example of the resulting station amplification terms. We then normalize individual event amplitude measurements for a given station prior to constructing the event-specific amplitude field and correction term.

Quality control checks are also applied prior to the construction of the amplitude field. We reject amplitude measurements greater than or less than a period dependent factor of the median amplitude calculated for all stations within 200 km of the station of interest

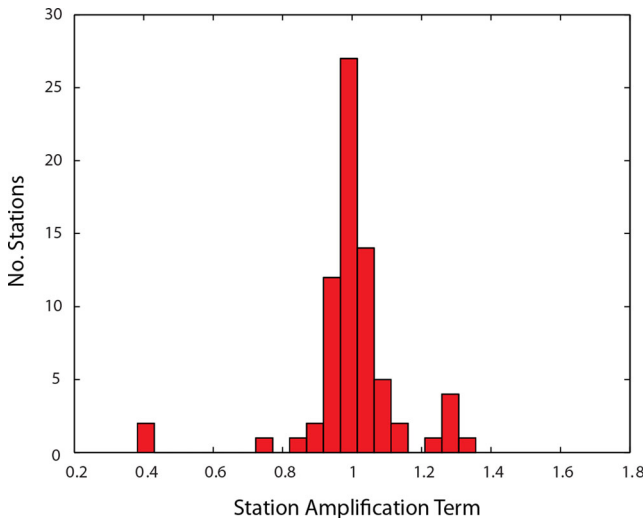


**Figure 4.** Example of determined station amplification terms at 40 s for entire network. The majority of the amplification terms hover around the expected value of 1. Stations with amplification terms  $>2$  or  $<0.2$  were not corrected for and their amplitude measurements were not used in determining the final structural phase velocity. The two stations with amplification terms of  $\sim 0.4$  are VWZM and KIFA. VWZM exhibits an amplification value at all periods of  $\sim 0.4$  which is related to uncertainties in the instrument response.

for each event. We chose this factor to be 2 at periods less than 60 s and 1.6 at periods greater than or equal to 60 s. This variation was determined after testing the influence of different values for the allowed amplification factor and identifying the value that would best reject outliers, while maintaining realistic variations in the amplitude field.

### 3.2 Ambient noise processing

We conducted ambient noise processing following the technique of Menke & Jin (2015), which aims to estimate the phase velocity from ambient-noise cross-correlograms in the frequency domain (termed cross-spectra) via waveform fitting using Aki's formula. We cut all available continuous data into 3 hr long windows with 50 per cent overlap, filtered the traces between 2 and 100 s, applied an amplitude

normalizing procedure to reduce the effects of earthquakes and other discrete signals (Bensen *et al.* 2007), and applied spectral whitening. Cross-correlating these traces for all available stations with inter-station distances  $>20$  km produced cross-spectra for 4200+ station pairs. Coherent Rayleigh waves are observed for nearly all stations including the lake-bottom instruments (Fig. 3b). We invert individual station-pair dispersion curves for maps of Rayleigh-wave phase velocity between 9 and 25 s following the inversion procedure used in Jin *et al.* (2015). This method performs the tomographic inversion via a generalized least-squares algorithm. We tested the influence of damping/smoothness choices in the inversion step and chose those parameters that provided the best fit to the data while maintaining realistic variations in phase velocity. Further information concerning the tomographic inversion of the ambient noise data (i.e. checkerboard tests for resolution, maps of the number of ray paths per grid cell and a comparison of the predicted phase velocity from the earthquake processing and ambient noise processing) can be found in the Supporting Information.

## 4 SPECIAL CONSIDERATIONS FOR LAKE-BOTTOM SEISMOMETERS

The addition of 6 broad-band lake-bottom seismometers (LBS) to the SEGMeNT experiment provides consistent station spacing across the axis of the Malawi Rift which lies beneath Lake Malawi (Fig. 1). This experiment is one of the only deployments of ocean-bottom seismometers (OBS) in a freshwater, lake environment. Additionally, Lake Malawi, as with other large African rift lakes, is characterized by a permanent temperature-induced density stratification and is anoxic below  $\sim 220$  m (Vollmer *et al.* 2005). Here, we present the first attempt to apply standard OBS processing techniques like compliance/tilt corrections and determination of instrument orientation to data acquired on instruments deployed in a lake. We apply these corrections prior to estimating phase velocity in the teleseismic band but find that the corrections are not required in the ambient noise period band (see below).

### 4.1 Noise characteristics and compliance corrections

Similar to ocean-bottom deployments, the LBS data suffer from higher noise levels than their onshore counterparts (Fig. 5) primarily

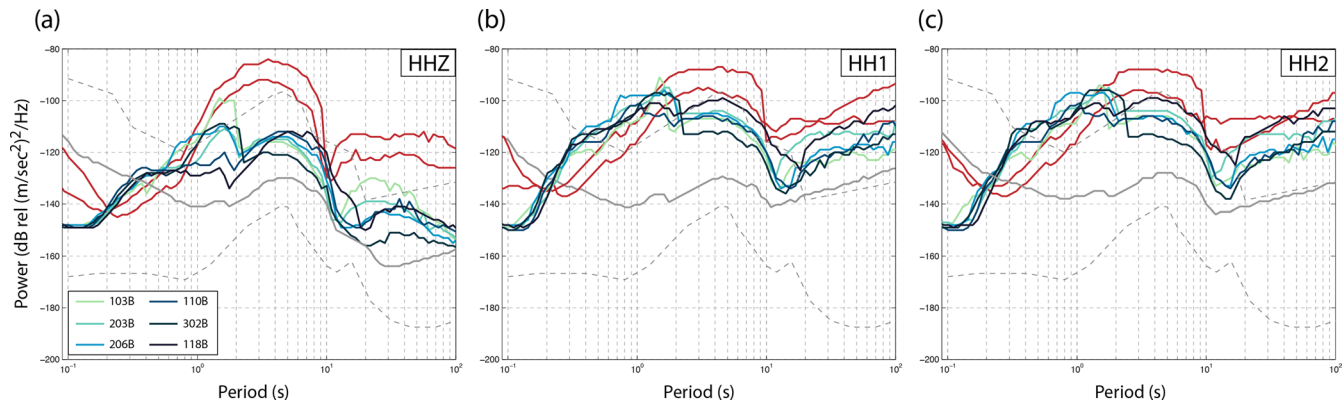


**Figure 5.** Comparison of noise power spectra for the six LBS in this study (light green to black lines) 2 Cascadia Initiative shielded OBS at  $\sim 350$  m water depth (red), and a representative onshore SEGMeNT station SCH (grey). The coloured lines show the average power spectra over 8 months for all instruments. The dashed grey lines indicate the Peterson high and low noise models. Spectra were acquired from the Modular Utility for STAtistical kNowledge Gathering (MUSTANG) system (Ahern *et al.* 2015). The spectra are shown for the (a) vertical component (HHZ), (b) horizontal component 1 (HH1) and (c) horizontal component 2 (HH2). The LBS are coloured according to water depth with the lightest colours representing the shallowest instruments (see inset in (a)). LBS water depths are given in Table 1.

**Table 1.** Water depths and locations of LBS used in this study. LBS are ordered from shallowest to deepest in terms of water depth.

LBS	Water depth (m)	Latitude	Longitude
103B	265	-9.716	34.112
203B	312	-10.031	34.158
206B	402	-9.912	34.320
110B	485	-10.322	34.396
302B	512	-10.853	34.310
118B	605	-11.214	34.430

due to the presence of additional noise sources like infragravity water waves, bottom currents and out-of-level sensors (e.g. Webb 1998). Fig. 5 shows a comparison of noise levels between the lake-bottom instruments used in this study (in 200–600 m of water, see Table 1), two shielded OBS in comparable water depths ( $\sim 350$  m) off the coast of Washington, USA (Toomey *et al.* 2014) and one of our nearby SEGMeNT onshore stations (SCH). Similar to the OBS, noise on the LBS on the vertical component at long period ( $T > 20$  s) is much higher than the nearby land station. Noise levels remain higher through the microseism peak, but then are much lower than the land station at short periods, where cultural noise dominates the onshore recordings. Noise levels for the LBS are lower than the comparable components of the OBS at nearly all periods, despite the fact that the LBS are not shielded. OBS studies have shown that on the vertical-component ground motion, long-period ( $T > 20$  s) noise often can be significantly reduced using observations of infragravity waves on the accompanying pressure gauge, and tilt inferred from the horizontals (Crawford & Webb 2000). These corrections are especially useful for deployments in shallow water where the strength of noise sources greatly increases (e.g. Webb 1998; Webb & Crawford 2010).

To identify noise sources, we calculated coherence between the pressure gauge, vertical and horizontal components (Fig. 6). This revealed high coherence between the vertical component and pressure gauge at periods between 20 and 80 s related to pressure gradients in the water column from long-wavelength infragravity waves. Little coherence was observed between the vertical and horizontal components suggesting that noise from bottom currents and/or poorly leveled sensors were not significant.

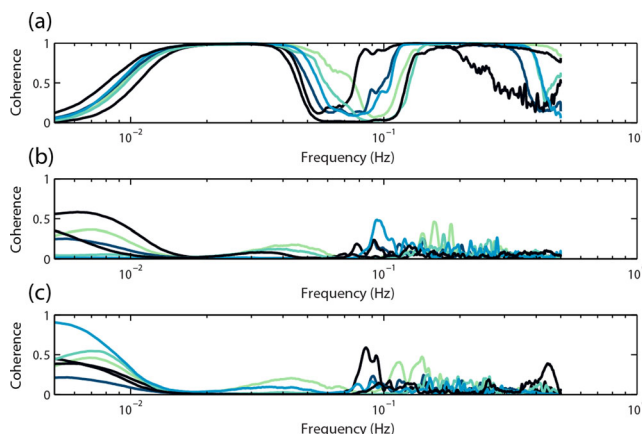


**Figure 6.** Coherence between the (a) vertical component and the differential pressure gauge, (b) horizontal component 1 and (c) horizontal component 2. Coherence was averaged for all broad-band LBS over the 8-month deployment. Data have been high-passed filtered with a corner at 0.005 Hz. Obvious influence from infragravity waves is apparent in the high coherence between the vertical and pressure gauges between 0.01 and 0.08 Hz. Refer to Fig. 5 for the colour scale used to identify individual LBS.

To remove the influence of noise resulting from infragravity waves, termed seafloor compliance, we followed the procedures of Webb & Crawford (1999). For each teleseismic event recorded on the LBS, we calculated the transfer function between the pressure gauge and vertical component for each instrument using 24 hr of continuous data from 1 or 2 d prior to the event of interest. To ensure that the continuous data from which the transfer functions were used did not include spurious noise or earthquakes, we cut the continuous data into 2 hr long windows and estimate the average power spectra. We discard any windows that lie outside the standard deviation of the mean, and we throw out the entire day of data if less than 10 windows are available. When the entire day of data is bad, we utilize the data from two days prior to the event. Transfer functions between the pressure and vertical components were calculated after stacking the resulting high-quality windows. The vertical component for each event is then corrected by subtracting the product of the transfer function and the observed seafloor pressure for the event. Figs 7 and 8 show the marked reduction in noise in both the frequency and time domain after applying these corrections. The noise from infragravity waves was not significant in the ambient noise band, so these traces do not require any correction.

#### 4.2 Determination of LBS orientations

We successfully determined the orientations for five out of the six LBS (instrument 110B recorded only one independent horizontal component, making orientation impossible to determine). To ensure robust orientation estimates, we employed both the earthquake orientation method of Stachnik *et al.* (2012) (hereafter termed Method 1) and the ambient noise orientation method of Zha *et al.* (2013, hereafter termed Method 2). Fig. 9 shows a comparison of the results from these two methods for instrument 103B. Both approaches rely on the same general principle of determining the orientation of the instrument by finding the rotation angle of the horizontal components that maximizes the coherence between the Rayleigh waves observed on the vertical component and the 90° phase-shifted Rayleigh waves on the rotated horizontal component. Table 2 gives a comparison of the results for all LBS from both methods. The two methods resulted in extremely consistent estimates of orientation with a mean difference of 1° and a maximum difference of 3.5°.

For Method 1, we used all events in our original catalogue with  $M_w > 6.5$  which resulted in 30 total events. However, given the high noise level on the horizontal components individual stations averaged only 7–10 high-quality events when determining the estimated orientation. Because of the small number of events used, gaps in azimuthal coverage were commonplace, motivating the use of Method 2 as an additional constraint. As a quality control check, we also employed Method 1 to confirm the orientations of stations in the onshore array and identified three misoriented sensors, demonstrating that orientation determination is a useful quality control measure for any onshore or offshore array.

Method 2 resembles that of Method 1 except that ambient-noise derived Rayleigh waves are substituted for their teleseismically derived counterparts. For a given station, daily CCFs are calculated in the time domain between the vertical and two horizontal components of the LBS of interest and the vertical components of all surrounding onshore stations (Fig. 9a). Given the large number of nearby high-quality onshore stations, we did not calculate CCFs for LBS-to-LBS station pairs. Our ability to depend on onshore-to-offshore station pairs is unique to this experiment as standard OBS deployments must rely solely on offshore-to-offshore station pairs

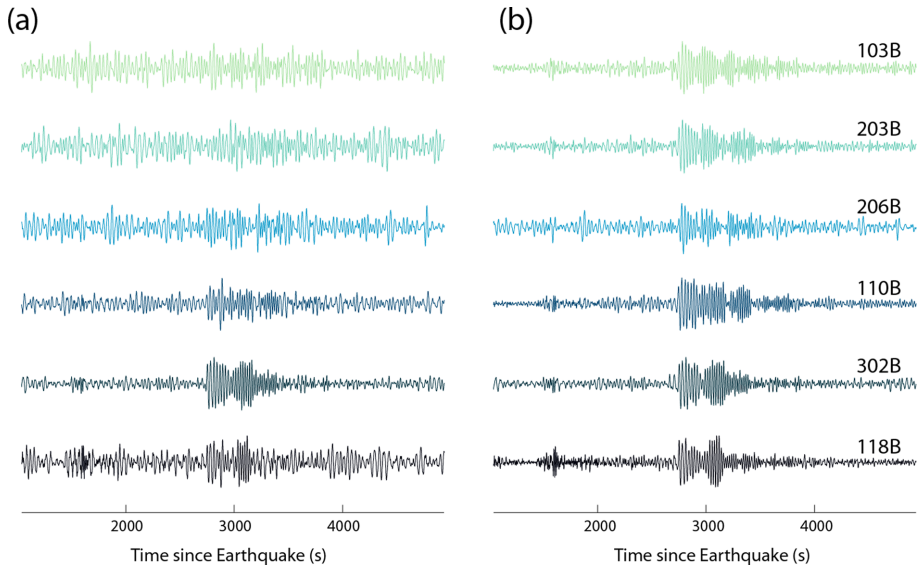


**Figure 7.** Comparison between original (left) and corrected (right) seismic traces recorded on LBS for the  $M_w$  6.4 event on 2015 July 3 in Yilkiqi, China (epicentral distance  $93.5^\circ$ ). The colours of the traces represent the individual instruments in both the left and right panels.

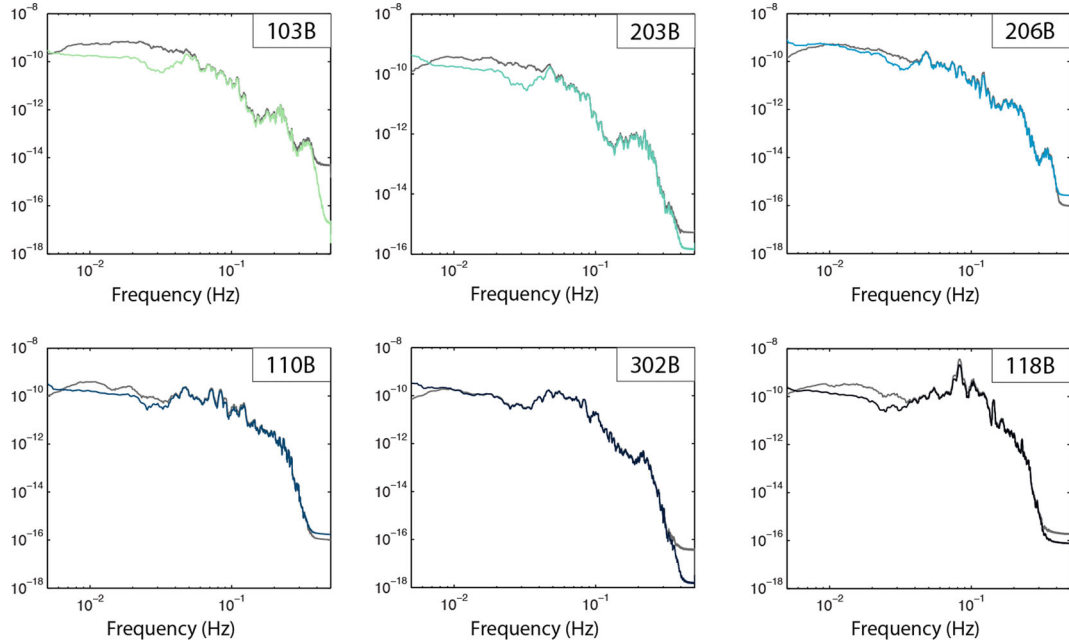


**Figure 8.** Comparison between the original (black) and corrected (coloured) power spectra for the earthquake shown in Fig. 5. Notable reduction in noise is observed between  $\sim 20$  and  $100$  s.

when using this orientation method. The large number of available station pairs led to excellent azimuthal coverage (Fig. 9b).

## 5 RESULTS AND DISCUSSION

Fig. 10 shows our preferred structural phase-velocity maps at periods of 9, 12, 18.5, 25, 40 and 60 s. Using a ray-theoretical approximation, we estimate that these maps satisfy approximately 80 per cent of the variance observed in the ambient-noise phase velocities, and 60 per cent of the variance in the individual ASWMS phase delays, compared to a regional 1-D starting model from the

nearby Rukwa rift (Kim *et al.* 2009). To guide our interpretation, we estimated fundamental-mode shear velocity sensitivity using the normal-mode summation code Mineos (Masters *et al.* 2007) for the periods of interest. The kernels are based on the Rukwa Rift model from Kim *et al.* (2009) with an adjusted crustal thickness of 34 km. This thickness is chosen to represent the thinner rift-central crustal thickness determined from SEGMeNT receiver functions by Borrego *et al.* (2015), which average  $38 \pm 4$  km. We find that all period bands are sensitive to the presence of a sedimentary layer at the top of the crust. Ambient-noise observations have high sensitivity down to  $\sim 35$  km depth and teleseismic observations down to  $> 150$  km (Fig. 11). We tested the influence of a water layer on the

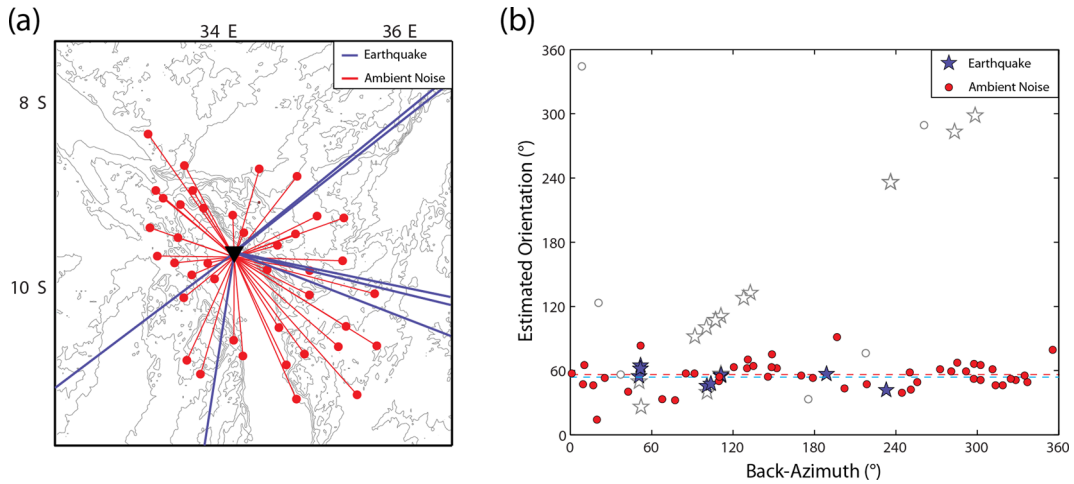


**Figure 9.** (a) Ray coverage map shown for orienting LBS 103B (location shown by black triangle). Red lines: interstation paths used in the ambient noise orientation method; blue lines: event-station great circle paths used in the earthquake orientation method. Topographic contours from NASA SRTM 30 m (Farr *et al.* 2007) are shown in grey. (b) Comparison of determined station orientation for 103B across backazimuth from ambient noise station pairs (red circles) and earthquakes (blue stars). Open symbols represent poor-quality measurements thrown out by both methods. The final determined orientations from these two methods are shown by the red and blue dashed lines, respectively.

**Table 2.** Final determined orientations for all LBS in the SEGMeNT experiment. Estimated orientations of horizontal component 1 (HH1) and their respective errors are shown for both the ambient-noise and earthquake orientation methods. We also present the determined orientation for the three misoriented onshore stations (MAND, MUDI and SCH). For these stations, the estimated orientation represents the orientation of the N component relative to true North.

Instrument	Estimated orientation from earthquakes (°)	Standard deviation (°)	Estimated orientation from ambient noise (°)	Standard deviation (°)
103B	54	5.5	54	9.9
110B	NA	NA	NA	NA
118B	28	3.6	29	19.0
203B	6	9.4	3	11.4
206B	56	6.4	55	13.6
302B	29	4.3	27	14.5
MAND	172	7.3	NA	NA
MUDI	175	9.9	NA	NA
SCH	175	9.3	NA	NA

sensitivity kernels and find that its presence slightly reduces overall sensitivities in the sediments and upper crust but does not change the overall distribution of sensitivity.

### 5.1 The North and Central basins of Lake Malawi: localization of sedimentation and extensional processes

At short periods, the strongest feature in our phase-velocity maps is the low-velocity area that follows the trend of the basins of Lake Malawi, oriented roughly N-S within the Central Basin and then rotating to NW-SE in the North Basin (Fig. 10). These low velocities are apparent at long periods (up to 40 s) but are strongest at periods <20 s, where Rayleigh-wave sensitivity is wholly within the sediments and crust. At the shortest periods, low velocities are seen in both the North and Central basins of Lake Malawi, but are 2–3 per cent slower in the Central Basin. We relate the low velocities at periods <20 s to the presence of a thick sedimentary package within Lake Malawi resulting from growth of border faults and related rift-floor subsidence, consistent with results of legacy and new reflection images, and possibly from the presence of older pre-rift strata.

Extension along border faults in strong lithosphere here results in flank uplift paired with deep, narrow, asymmetric rift basins (e.g. Morley 1988; Ebinger *et al.* 1991). Ebinger *et al.* (1993) simulated the basin and flank morphology and free-air gravity anomaly patterns across the North Basin with 4–6 km of low-density sedimentary strata. Additionally, predictive models of airborne gravity and magnetic data in the onshore region of the North Basin indicate sediments are 4–4.5 km thick (Macgregor 2015).

Fewer estimates of sedimentary thickness exist for the Central Basin compared to the North Basin (Scholz *et al.* 1989). However, given that the Central Basin exhibits the greatest water depths within Lake Malawi and is the terminus for two major rivers, the S. Rukuru and Ruhuhu, the Neogene-recent sediment package here is likely to be as thick or thicker than that in the North Basin. If the 3 per cent reduction in velocity in the Central Basin relative to the North Basin is due to syn-rift sediment, then this would require an increase in the thickness of basin sediments, and thus could imply an increase in total extension, from north to south. Alternatively, the Central Basin is also thought to contain several kilometres of Karoo super-group sediments (Ebinger *et al.* 1987; Mortimer *et al.* 2016), which are exposed onshore in the Ruhuhu basin (Kreuser *et al.* 1990) and could contribute significantly to the strong short-period

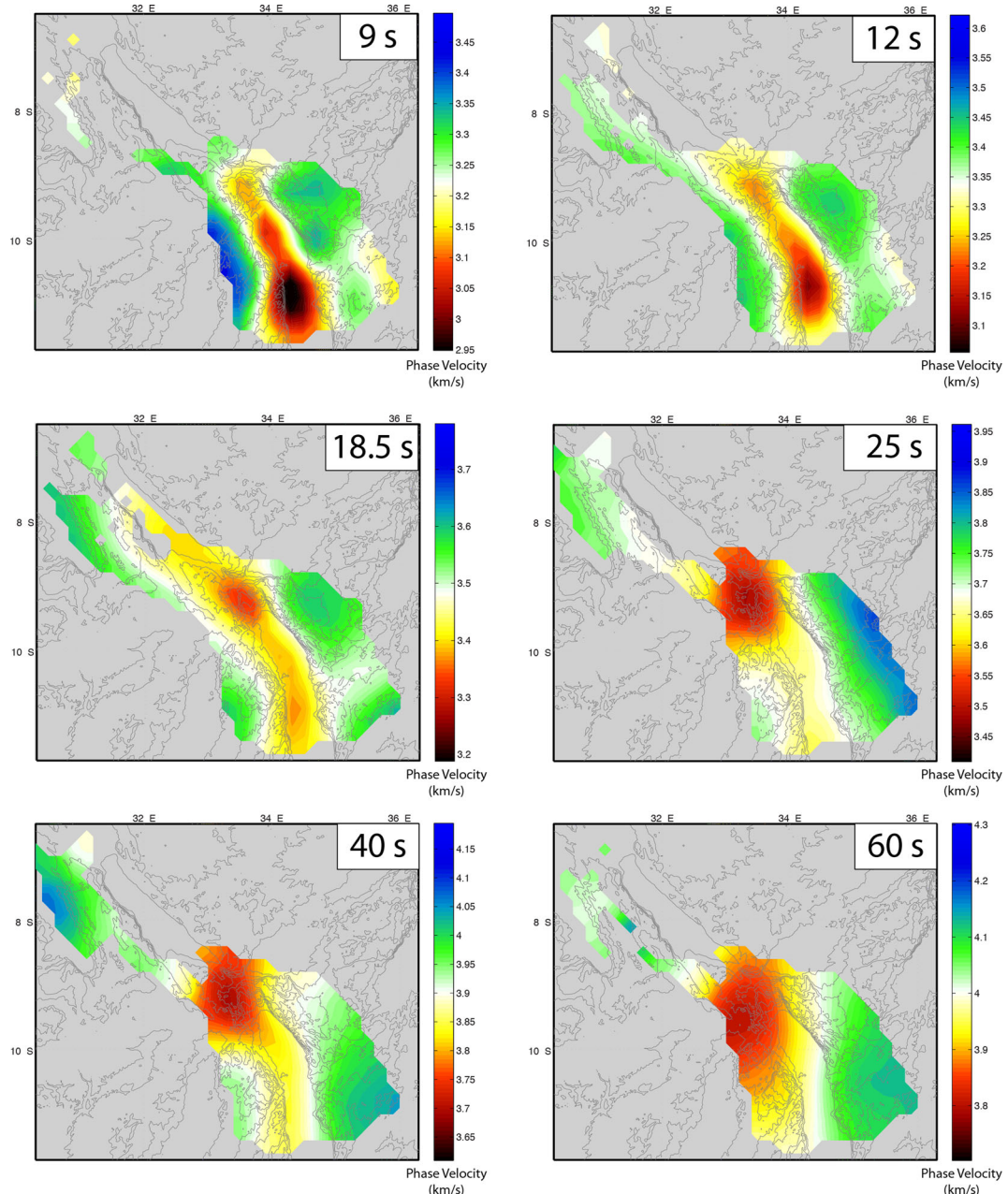


**Figure 10.** Maps of phase velocity for ambient noise (9, 12 and 18.5 s) and teleseismic (25, 40 and 60 s) Rayleigh waves. The period of the phase-velocity measurement is labeled in the top right corner of each map.

velocity anomaly. Several lines of evidence point to the presence of Karoo sediments in the Central Basin including a transition in the character of seismic reflectors between the North and Central basins (Ebinger *et al.* 1987) and the location/orientation of horsts within the Central Basin which are thought to be controlled by pre-existing structures associated with Karoo rifting (Mortimer *et al.* 2016). Additionally, preliminary observations from the SEGMeNT active-source refraction study report a significant increase in the crossover distance between sedimentary and crustal refractions in the Central Basin (Accardo *et al.* 2016), and preliminary *P*-wave velocity models contain a several kilometres thick layer with *P*-wave velocities between 3 and 5 km s<sup>-1</sup>, which may be consistent with older, more indurated Karoo sediments (Shillington *et al.* 2015). We suggest that the low-velocity anomaly within the Central Basin represents an increased sediment package resulting from both greater sediment

deposition related to Neogene-recent rifting (Mortimer *et al.* 2016) as well as the presence of several kilometres of Karoo-age sediment.

Further support for the contribution of Karoo sediments to the low velocities in the Central Basin is provided by the observation of a low-velocity region extending from the eastern margin of the Central Basin onshore, where it directly underlies the Ruhuhu basin. This anomaly is subtler than those associated with the RVP and lake basins relative to the plateaus, but is a persistent feature at periods less than 25 s, and we interpret it as arising from Karoo sedimentary facies.

Our phase-velocity maps show that the low velocities beneath Lake Malawi extend to longer periods where the primary sensitivity is well below the depth of the sedimentary basin, in particular relative to the eastern margin of the rift, where high velocities persist at all frequencies (Fig. 12b). While these slow velocities likely are

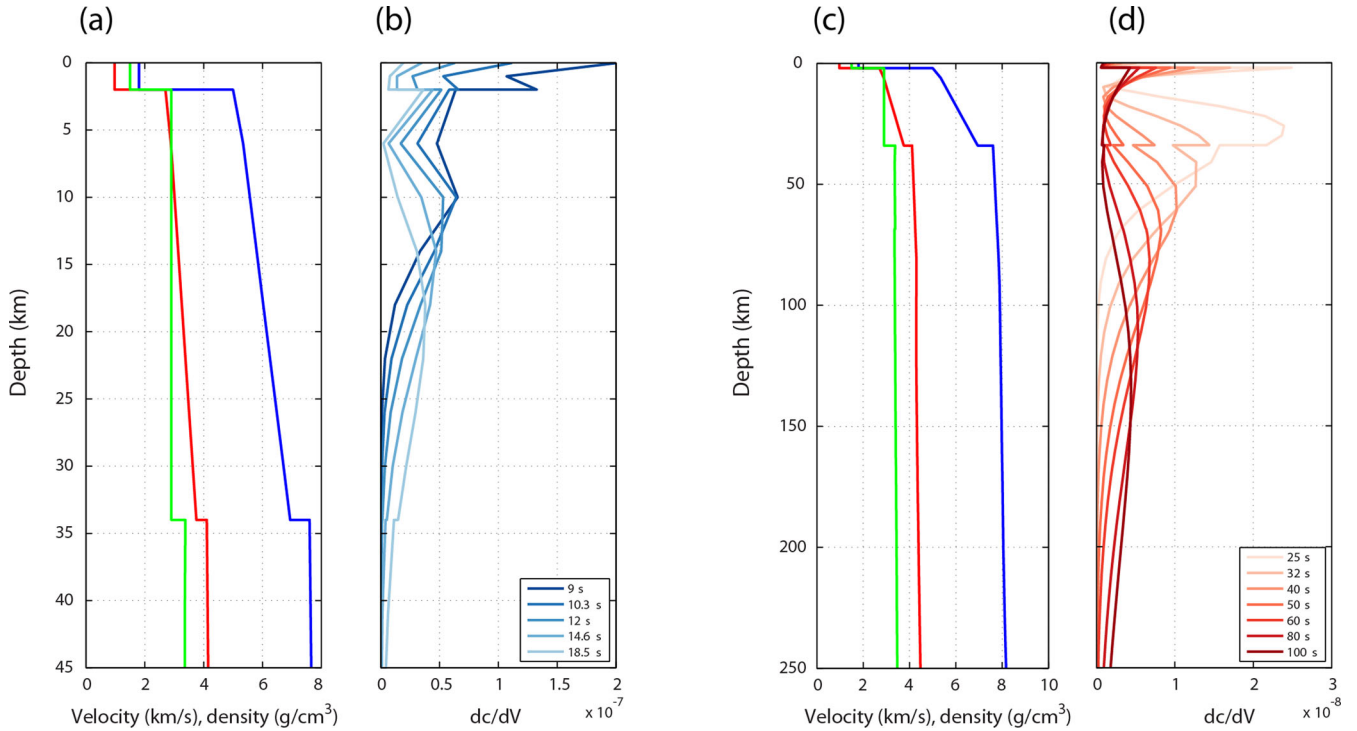


**Figure 11.** Comparison of phase-velocity sensitivity kernels for the Earth model based off of the study by Kim *et al.* (2009). (a) and (c) show  $P$ -wave velocity in blue, density in green, and  $S$ -wave velocity in red. (b) Sensitivity for the ambient noise period band down to a depth of 45 km. (d) Sensitivity for the teleseismic period band down to a depth of 250 km. Note that the  $x$ -axes changes scale between (a) and (b), and (c) and (d). Sensitivity kernels were calculated using the normal-mode programme Mineos (Masters *et al.* 2007).

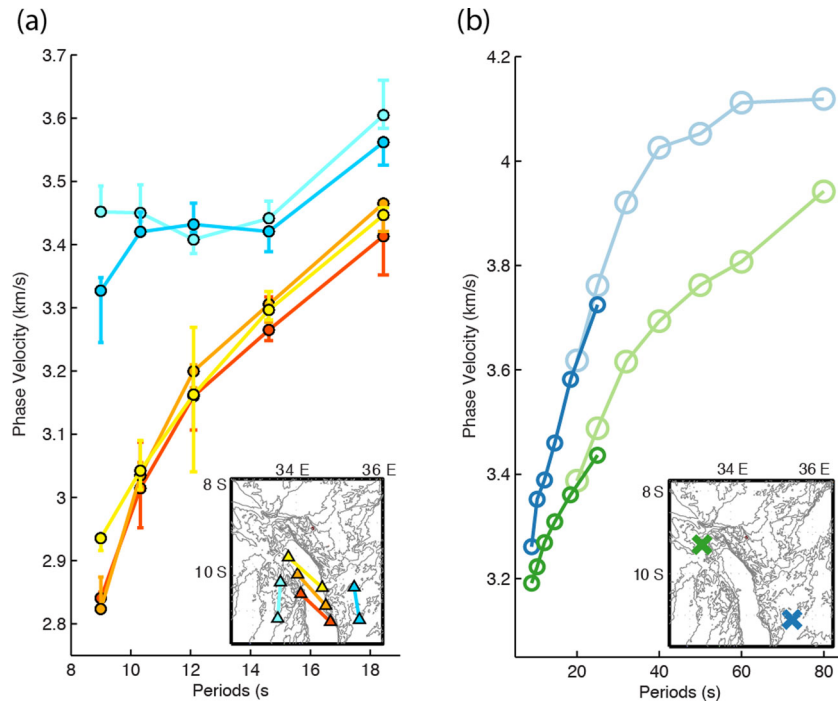


**Figure 12.** Comparison of (a) individual ambient-noise station-pair dispersion curves and (b) inverted phase-velocity curves from ambient-noise and teleseismic data sets. (a) Estimated dispersion curves determined from individual station pairs. Locations of station pairs are shown in the inset map with same colour as the dispersion curves. Warmer colours represent station pairs associated with paths crossing the Central Basin of Lake Malawi, while cooler colours represent station pairs associated with paths on the western and eastern plateaus. (b) Comparison of estimated phase velocities from teleseismic (lighter colours) and ambient noise (darker colours) at two locations.

partly controlled by the sedimentary structure, the fact that they roughly follow the trend of the primary rift basin but are broader than the short-period basin features at periods suggest velocity reduction in the middle to lower crust. Fig. 12(a) compares dispersion curves estimated from station pairs with paths crossing the Central Basin and paths wholly within the western and eastern plateaus. The difference in seismic velocities between the rift axis and the surrounding plateaus is  $\sim 2$  per cent at 18.5 s and decreases with increasing period until ultimately at 50 s, the anomaly is subsumed into the broad region of low velocities within the western half of the study region (Fig. 10).

A reduction in velocities beneath the rift at periods sensitive to the crust and uppermost mantle could be explained by localized fracturing and deformation associated with extension (Carlson & Gangi 1985) or elevated temperatures. These observations are counter to what is observed in magmatic rifts, where lower crustal velocities are higher beneath the rift than outside it owing to extensive magmatic intrusion to the lower and middle crust (e.g. Birt *et al.* 1997; Hamblon *et al.* 2007) or significant crustal thinning, where slow crustal material is replaced by denser, faster velocity upper-mantle material. A reduction in velocities at longer periods would be expected if lithospheric thinning has occurred such that higher velocity lithospheric mantle is replaced by slower, hotter asthenospheric mantle that may contain a small melt fraction. In detail this low-velocity anomaly is shifted slightly westward from the true centre of Lake Malawi, persisting farther west beneath the Nyika plateau as compared to the abrupt transition to fast velocities at the junction beneath the eastern boundary of the lake and the eastern plateau. The asymmetry in crustal velocities may relate to the presence of heterogeneous pre-existing crustal terrains, asymmetric rifting processes, or some combination of the two. The competing effects of variations in crustal thickness and crustal and upper-mantle velocity structure can be difficult to distinguish using phase-velocity maps derived from surface waves, which are defined by integrative depth sensitivity. Future analyses that utilize independent constraints on basin and crustal architecture will clarify the nature of crustal and lithosphere extension.

## 5.2 The Rungwe Volcanic Province: the localization of magmatism at depth

One of the most striking features in the phase-velocity maps in Fig. 10 is the prominent low-velocity region imaged beneath the RVP. We find that the anomaly has the strongest amplitude within an intermediate period band ( $\sim 25$ – $60$  s) and becomes more diffuse and shifts westwards at longer periods. Phase velocities for this low-velocity region are  $\sim 5$  per cent lower than the surrounding western and eastern plateaus at intermediate and long periods. At periods between 25 and 50 s, the anomaly appears roughly circular, with the lowest velocities confined to a region with a radius of  $\sim 70$  km. The ray coverage provided by the TANGA stations allows clear imaging of the north/northwest edge of the feature, suggesting that it does not extend beyond the narrow Songwe basin into the Rukwa rift segment. The anomaly decreases in size and amplitude within the ambient-noise period band.

Our phase-velocity images place the strongest anomaly at periods that suggest a lower lithosphere or asthenospheric origin for the RVP low-velocity feature. The localization of this large-magnitude, low-velocity anomaly beneath the RVP matches lower resolution observations of low-velocity regions associated with the RVP (O'Donnell *et al.* 2016) and other volcanic provinces along the Western Branch

(Adams *et al.* 2012; O'Donnell *et al.* 2013). Although Western-rift eruptive centres commonly coincide with intrabasinal accommodation zones, our new results and earlier models suggest that the localization of magma is caused by processes at depth (Ruppel 1995; Corti *et al.* 2002; Corti 2004). The *ca.* 20 My time span of magmatism and regional elevation of magmatic provinces suggests they are temporally persistent, and could have played a role in strain localization. Localized melting may be expected to occur beneath the Rungwe region due to a variety of mechanisms including thermal or compositional anomalies in the upper mantle, thinning of the lithosphere from Neogene-recent rifting, pre-thinning of the lithosphere prior to present rifting, or a combination of the above.

Ebinger & Sleep (1998) model the flow of upwelling mantle plume beneath variable thickness lithosphere, and predict enhanced melting beneath the margins of the deeply rooted Tanzania and Congo cratons. Regions of pre-existing weakness and/or thin lithosphere are proposed to control lateral transport of hot plume material and where it ponds and escapes to the surface as a volcanic centre, as seen along the Western Branch (e.g. Nyblade *et al.* 2000). Studies of shear wave splitting further promote the idea of broad scale along-axis mantle flow beneath the EARS (Bagley & Nyblade 2013; Tepp 2016), although pre-existing lithospheric fabrics may also play a role (Walker *et al.* 2004). Our observations of highly focused low velocities beneath the long-lived RVP and absence of similarly low velocities beneath the rift basins to the north and the south suggest that along-axis flow may not be as significant in this part of the EAR (Fig. 10). Decreased velocities are present beneath the axis of the Malawi Rift at the same periods where the RVP anomaly appears strongest but these velocities are appreciably higher relative to the surrounding plateau than those observed beneath the RVP ( $\sim 2.5$  and  $\sim 5$  per cent, respectively).

At the longest periods, the slow velocities associated with the RVP show a broadening and westward expansion at depth compared with the focusing of low velocities beneath Rungwe volcanoes at shorter periods (Figs 10 and 12). A similar broadening and westward shift in the location of the RVP anomaly is observed in the Rayleigh-wave phase-velocity maps of both Adams *et al.* (2012) and O'Donnell *et al.* (2013). The observation of low velocities at depth outside the rift valley and volcanic province is qualitatively similar to observations from the Main Ethiopian Rift (MER), where low velocities extend west beneath the Ethiopian Plateau at depths  $> 75$  km (Bastow *et al.* 2008; Gallacher *et al.* 2016). However, the absolute phase velocities are substantially lower ( $> 5$  per cent) within the MER (Gallacher *et al.* 2016) at all periods compared to those in the Malawi Rift. We suggest the westward broadening of the observed anomaly at lower lithospheric depths may represent a broad region of lithospheric thinning associated with extension and/or a broad region of relatively warm asthenosphere underlying the rift and the western plateau.

## 6 CONCLUSIONS

This study presents the first locally constrained tomographic phase-velocity maps of the weakly extended Malawi Rift and surrounding region. We have successfully corrected six LBS for long-period infragravity waves and robustly determined their orientations. This effort represents some of the first observations of seismometer derived noise levels in a freshwater rather than oceanic environment. Our resulting phase-velocity maps present two views of the rift system. At the shortest periods and hence shallowest depths, low velocities are bounded to the North and Central basins as a result of

thick sedimentary packages. Low velocities beneath the lake basins extend to 40 s, where sensitivities are within the lower crust and potentially uppermost lithospheric mantle suggesting a localization of extensional processes. At the longest periods, our phase-velocity images reveal a ubiquitous low-velocity region associated with the RVP and the colocated accommodation zone. Our data provide excellent ray coverage such that we can constrain the RVP anomaly and show that similar-magnitude low-velocity regions do not extend north into the Rukwa Rift or south along the Malawi Rift. Estimates of phase-velocity sensitivity place these low velocities within the lithospheric mantle and potentially uppermost asthenosphere, suggesting that mantle processes may control the association of volcanic centres and the localization of magmatism.

## ACKNOWLEDGEMENTS

The authors gratefully acknowledge all of those involved in the acquisition of the SEGMeNT and TANGA data sets, including technicians and engineers from PASSCAL program of the Incorporated Research Institutions in Seismology (IRIS) and the OBS program at Scripps Institution of Oceanography and the crews of the F/V *Ndunduma* and M/V *Chilembwe*. We thank the communities in our study area and national and regional governmental entities for their support, without which our project would not have been possible. Seismic instrumentation was obtained from IRIS-PASSCAL, and the Ocean Bottom Seismology Instrumentation Program (OBSIP). Data are archived at the IRIS Data Management Center, and was downloaded using the Standing Order for Data (SOD) software package out of the University of South Carolina. We thank Ge Jin, Yang Zha, PeiYing Lin and Helen Janiszewski for sharing computer programs used in this study and Cornelia Class and Gary Mesko for useful discussions. This research was supported by National Science Foundation (NSF) grant EAR-1110921, the NSF Graduate Research Fellowship Programme, Natural Environment Research Council (NERC) grant NE/K500926/1 and NERC grant NE/L013932/1. Seismic equipment from SEIS-UK is funded by NERC under agreement R8/H10/64 and funding was provided by Beach Petroleum.

## REFERENCES

- Accardo, N.J. *et al.*, 2016. Constraints on the 3D sediment and crustal architecture of the weakly extended Malawi Rift from the onshore/offshore wide-angle refraction experiment, *EOS, Trans. Am. geophys. Un.*, Fall Meet. Suppl.
- Adams, A., Nyblade, A. & Weeraratne, D., 2012. Upper mantle shear wave velocity structure beneath the East African plateau: evidence for a deep, plateau-wide low velocity anomaly, *Geophys. J. Int.*, **189**, 123–142.
- Ahern, T., Benson, R., Casey, R., Trabant, C. & Weertman, B., 2015. Improvements in data quality, integration and reliability: new developments at the IRIS DMC, *Adv. Geosci.*, **40**, 31–35.
- Armitage, J.J., Ferguson, D.J., Goes, S., Hammond, J.O.S., Calais, E., Rychert, C.A. & Harmon, N., 2015. Upper mantle temperature and the onset of extension and break-up in Afar, Africa, *Earth planet. Sci. Lett.*, **418**, 78–90.
- Bagley, B. & Nyblade, A.A., 2013. Seismic anisotropy in eastern Africa, mantle flow, and the African superplume, *Geophys. Res. Lett.*, **40**, 1500–1505.
- Bastow, I.D. & Keir, D., 2011. The protracted development of the continent-ocean transition in Afar, *Nat. Geosci.*, **4**, 248–250.
- Bastow, I.D., Nyblade, A.A., Stuart, G.W., Rooney, T.O. & Benoit, M.H., 2008. Upper mantle seismic structure beneath the Ethiopian hot spot: rifting at the edge of the African low-velocity anomaly, *Geochem. Geophys. Geosyst.*, **9**, 1–25.
- Begg, G.C. *et al.*, 2009. The lithospheric architecture of Africa: seismic tomography, mantle petrology, and tectonic evolution, *Geosphere*, **5**, 23–50.
- Bensen, G.D., Ritzwoller, M.H., Barmin, M.P., Levshin, A.L., Lin, F., Moschetti, M.P., Shapiro, N.M. & Yang, Y., 2007. Processing seismic ambient noise data to obtain reliable broad-band surface wave dispersion measurements, *Geophys. J. Int.*, **169**, 1239–1260.
- Birt, C.S., Maguire, P.K.H., Khan, M.A., Thybo, H., Keller, G.R. & Patel, J., 1997. The influence of pre-existing structures on the evolution of the southern Kenya Rift Valley evidence from seismic and gravity studies, *Tectonophysics*, **278**, 211–242.
- Borrego, D. *et al.*, 2015. Crustal structure in Northern Malawi and Southern Tanzania surrounding Lake Malawi and the Rungwe Volcanic Province, *EOS, Trans. Am. geophys. Un.*, Fall Meet. Suppl.
- Bott, M.H.P., 1991. Ridge push and associated plate interior stress in normal and hot spot regions, *Tectonophysics*, **200**, 17–32.
- Buck, W.R., 2004. Consequences of asthenospheric variability on continental rifting, in *Rheology and Deformation of the Lithosphere at Continental Margins*, eds Karner, G.D., Taylor, B.N., Drosdoff, W. & Kohlstedt, D.L., pp. 1–30, Columbia Univ. Press, New York.
- Buck, W.R., 2006. The role of magma in the development of the Afro-Arabian Rift System, in *The Afar Volcanic Province Within the East African Rift System*, eds Yirgu, G., Ebinger, C.J. & Maguire, P.K.H., pp. 43–54, Geological Society of London, Special Publications.
- Carlson, R.I. & Gangi, A.I., 1985. Effect of cracks on the pressure-dependence of *P*-wave velocities in crystalline rocks, *J. geophys. Res.*, **90**, 8675–8684.
- Catuneanu, O., Wopfner, H., Eriksson, P.G., Cairncross, B., Rubidge, B.S., Smith, R.M.H. & Hancox, P.J., 2005. The Karoo basins of south-central Africa, *J. Afr. Earth. Sci.*, **43**, 211–253.
- Chorowicz, J., 2005. The East African rift system, *J. Afr. Earth. Sci.*, **43**, 379–410.
- Corti, G., 2004. Centrifuge modelling of the influence of crustal fabrics on the development of transfer zones: insights into the mechanics of continental rifting architecture, *Tectonophysics*, **384**, 191–208.
- Corti, G., Bonini, M., Mazzarini, F., Boccaletti, M., Innocenti, F., Manetti, P., Mulugeta, G. & Sokoutis, D., 2002. Magma-induced strain localization in centrifuge models of transfer zones, *Tectonophysics*, **348**, 205–218.
- Corti, G., Bonini, M., Conticelli, S., Innocenti, F., Manetti, P. & Sokoutis, D., 2003. Analogue modelling of continental extension: a review focused on the relations between the patterns of deformation and the presence of magma, *Earth-Sci. Rev.*, **63**, 169–247.
- Crossley, R. & Crow, M.J., 1980. *The Malawi Rift, in Geodynamic Evolution of the Aft'o-Arabian Rift System*, pp. 77–87, Accademia Nazionale Lincei, Rome.
- Craig, T.J., Jackson, J.A., Priestley, K. & McKenzie, D., 2011. Earthquake distribution patterns in Africa: their relationship to variations in lithospheric and geological structure, and their rheological implications, *Geophys. J. Int.*, **185**, 403–434.
- Crawford, W.C. & Webb, S.C., 2000. Identifying and removing tilt noise from low-frequency (<0.1 Hz) seafloor vertical seismic data, *Bull. seism. Soc. Am.*, **90**, 952–963.
- Dugda, M.T., Nyblade, A.A., Julia, J., Langston, C.A., Ammon, C.J. & Simiyu, S., 2005. Crustal structure in Ethiopia and Kenya from receiver function analysis: implications for rift development in eastern Africa, *J. geophys. Res.*, **110**, B01303, doi:10.1029/2004JB003065.
- Ebinger, C.J. & Sleep, N.H., 1998. Cenozoic magmatism throughout east Africa resulting from impact of a single plume, *Nature*, **395**, 788–791.
- Ebinger, C.J. & Casey, M., 2001. Continental breakup in magmatic provinces: an Ethiopian example, *Geology*, **29**, 527–535.
- Ebinger, C.J., Deino, A.L., Drake, E. & Tesha, A.L., 1989. Chronology of volcanism and rift basin propagation: Rungwe Volcanic Province, East Africa, *J. geophys. Res.*, **94**, 15785–15803.
- Ebinger, C.J., Rosendahl, B.R. & Reynolds, D.J., 1987. Tectonic model of the Malawi rift, Africa, *Tectonophysics*, **141**, 215–235.

- Ebinger, C.J., Karner, G.D. & Weiszel, J.K., 1991. Mechanical strength of extended continental lithosphere—constraints from the Western Rift System, East-Africa, *Tectonics*, **10**, 1239–1256.
- Ebinger, C.J., Deino, A.L., Tesha, A.L., Becker, T. & Ring, U., 1993. Tectonic controls on rift basin morphology: evolution of the northern Malawi (Nyasa) Rift, *J. geophys. Res.*, **98**, 17 821–17 836.
- Farr, T.G. et al., 2007. The Shuttle radar topography mission, *Rev. Geophys.*, **45**, RG2004, doi:10.1029/2005RG000183.
- Fagereng, A., 2013. Fault segmentation, deep rift earthquakes and crustal rheology: Insights from the 2009 Karonga sequence and seismicity in the Rukwa–Malawi rift zone, *Tectonophysics*, **601**, 216–225.
- Fishwick, S., 2010. Surface wave tomography: imaging of the lithosphere–asthenosphere boundary beneath central and southern Africa?, *Lithos*, **120**, 63–73.
- Fontijn, K., Delvaux, D., Ernst, G.G.J., Kervyn, M., Mbede, E. & Jacobs, P., 2010a. Tectonic control over active volcanism at a range of scales: case of the Rungwe Volcanic Province, SW Tanzania; and hazard implications, *J. Afr. Earth Sci.*, **58**, 764–777.
- Fontijn, K., Ernst, G.G.J., Elburg, M.A., Williamson, D., Abdallah, E., Kwelwa, S., Mbede, E. & Jacobs, P., 2010b. Holocene explosive eruptions in the Rungwe Volcanic Province, Tanzania, *J. Volc. Geotherm. Res.*, **196**, 91–110.
- Fontijn, K., Williamson, D., Mbede, E. & Ernst, G.G.J., 2012. The Rungwe Volcanic Province, Tanzania—a volcanological review, *J. Afr. Earth Sci.*, **63**, 12–31.
- Forsyth, D. & Uyeda, S., 1975. On the relative importance of the driving forces of plate motion, *Geophys. J. Int.*, **43**, 163–200.
- Furman, T., 2007. Geochemistry of East African Rift basalts: an overview, *J. Afr. Earth Sci.*, **48**, 147–160.
- Gallacher, R.J. et al., 2016. The initiation of segmented buoyancy driven melting during continental breakup, *Nat. Commun.*, **7**, doi:10.1038/ncomms13110.
- Hamblock, J.M., Andronicos, C.L., Miller, K.C., Barnes, C.G., Ren, M.H., Averill, M.G. & Anthony, E.Y., 2007. A composite geologic and seismic profile beneath the southern Rio Grande rift, New Mexico, based on xenolith mineralogy, temperature, and pressure, *Tectonophysics*, **442**, 14–48.
- Jackson, J. & Blenkinsop, T., 1993. The Malawi earthquake of March 10, 1989: deep faulting within the East African Rift System, *Tectonics*, **12**, 1131–1139.
- Jin, G. & Gaherty, J.B., 2015. Surface wave phase-velocity tomography based on multichannel cross-correlation, *Geophys. J. Int.*, **201**, 1383–1398.
- Jin, G., Gaherty, J.B., Abbers, G.A., Kim, Y., Eilon, Z. & Buck, W.R., 2015. Crust and upper mantle structure associated with extension in the Woodlark Rift, Papua New Guinea from Rayleigh-wave tomography, *Geochem. Geophys. Geosys.*, **16**(11), 3808–3824.
- Kendall, J.-M., Stuart, G.W., Ebinger, C.J., Bastow, I.D. & Keir, D., 2005. Magma-assisted rifting in Ethiopia, *Nature*, **433**, 146–148.
- Kim, S., Nyblade, A.A. & Baag, C.E., 2009. Crustal velocity structure of the Rukwa Rift in the Western Branch of the East African Rift System, *S. Afr. J. Geo.*, **112**(3–4), 251–260.
- Kreuser, T., Wopfner, H., Kaaya, C.Z., Markwort, S., Semkiwa, P.M. & Aslandis, P., 1990. Depositional evolution of Permo-Triassic Karoo basins in Tanzania with reference to their economic potential, *J. Afr. Earth Sci.*, **10**, 151–167.
- Lin, F.-C. & Ritzwoller, M.H., 2011. Helmholtz surface wave tomography for isotropic and azimuthally anisotropic structure, *Geophys. J. Int.*, **186**(3), 1104–1120.
- Lin, F.-C., Ritzwoller, M.H. & Snieder, R., 2009. Eikonal tomography: surface wave tomography by phase front tracking across a regional broadband seismic array, *Geophys. J. Int.*, **177**, 1091–1110.
- Masters, G., Barmine, M. & Kientz, S., 2007. *Mineos Users' manual*, Computational Infrastructure for Geodynamics, Pasadena.
- Macgregor, D., 2015. History of the development of the East African Rift System: a series of interpreted maps through time, *J. Afr. Earth Sci.*, **101**, 232–252.
- Menke, W. & Jin, G., 2015. Waveform fitting of cross spectra to determine phase velocity using Aki's formula, *Bull. seism. Soc. Am.*, **105**, 1619–1627.
- Morley, C.K., 1988. Variable extension in Lake Tanganyika, *Tectonics*, **7**, 785–801.
- Mortimer, E.J., Paton, D.A., Scholz, C.A. & Strecker, M.R., 2016. Implications of structural inheritance in oblique rift zones for basin compartmentalization: Nkhata Basin, Malawi Rift (EARS), *Mar. Petrol. Geol.*, **72**, 110–121.
- Mulibio, G.D. & Nyblade, A.A., 2013. The P and S wave velocity structure of the mantle beneath eastern Africa and the African superplume anomaly, *Geochem. Geophys. Geosyst.*, **14**, 2696–2715.
- Nyblade, A.A., Owens, T.J., Gurrola, H., Ritsema, J. & Langston, C.A., 2000. Seismic evidence for a deep upper mantle thermal anomaly beneath east Africa, *Geology*, **28**, 599–602.
- O'Donnell, J.P., Adams, A., Nyblade, A.A., Mulibio, G.D. & Tugume, F., 2013. The uppermost mantle shear wave velocity structure of eastern Africa from Rayleigh wave tomography: constraints on rift evolution, *Geophys. J. Int.*, **194**, 961–978.
- O'Donnell, J.P., Selway, K., Nyblade, A.A., Brazier, R.A., Tahir, N.E. & Durrheim, R.J., 2016. Thick lithosphere, deep crustal earthquakes and no melt: a triple challenge to understanding extension in the western branch of the East African Rift, *Geophys. J. Int.*, **204**(2), 985–998.
- Pasyanos, M.E. & Nyblade, A.A., 2007. A top to bottom lithospheric study of Africa and Arabia, *Tectonophysics*, **444**, 27–44.
- Roberts, E.M. et al., 2012. Initiation of the western branch of the East African Rift coeval with the eastern branch, *Nat. Geosci.*, **5**(4), 289–294.
- Rosendahl, B.R., Kilembe, E. & Kaczmarick, K., 1992. Comparison of the Tanganyika, Malawi, Rukwa and Turkana Rift Zones from analyses of seismic-reflection data, *Tectonophysics*, **213**, 235–256.
- Ruppel, C., 1995. Extensional processes in continental lithosphere, *J. geophys. Res.*, **100**, 24 187–24 215.
- Saria, E., Calais, E., Stamps, D.S., Delvaux, D. & Hartnady, C.J.H., 2014. Present-day kinematics of the East African Rift, *J. geophys. Res.*, **119**, 3584–3600.
- Scholz, C.A. & Rosendahl, B.R., 1988. Low lake stands in Lakes Malawi and Tanganyika, East Africa, delineated with multifold seismic data, *Science*, **240**, 1645–1648.
- Scholz, C.A., Rosendahl, B.R., Versfelt, J., Kaczmarick, K.J. & Woods, L.D., 1989. *Seismic Atlas of Lake Malawi*, Project PROBE, p. 116, Duke University.
- Shillington, D.J. et al., 2015. Active-source seismic imaging below Lake Malawi (Nyasa) from the SEGMeNT project, *EOS, Trans. Am. geophys. Un.*, Fall Meet. Suppl.
- Shillington, D.J. et al., 2016. Acquisition of a unique onshore/offshore geological and geochemical dataset in the Northern Malawi (Nyasa) Rift, *Seismol. Res. Lett.*, **87**(6), 1–11.
- Specht, T.D. & Rosendahl, B.R., 1989. Architecture of the Lake Malawi Rift, East Africa, *J. Afr. Earth Sci.*, **8**, 355–382.
- Stachnik, J.C., Sheehan, A.F., Zietlow, D.W., Yang, Z., Collins, J. & Ferris, A., 2012. Determination of New Zealand ocean bottom seismometer orientation via Rayleigh-wave polarization, *Seismol. Res. Lett.*, **83**(4), 704–713.
- Tepp, G., 2016. Seismic analysis of magmatism in the Galápagos Archipelago And East Africa, *PhD thesis*, University of Rochester, Rochester, NY.
- Toomey, D.R. et al., 2014. The Cascadia Initiative: a sea change in seismological studies of subduction zones, *Oceanography*, **27**(2), 138–150.
- Van Avendonk, H.J.A., Lavier, L.L., Shillington, D.J. & Manatschal, G., 2009. Extension of continental crust at the margin of the eastern Grand Banks, Newfoundland, *Tectonophysics*, **468**, 131–148.
- Vollmer, M.K., Bootsma, H.A., Hecky, R.E., Patterson, G., Halfman, J.D., Edmond, J.M., Eccles, D.H. & Weiss, R.F., 2005. Deep-water warming trend in Lake Malawi, East Africa, *Limnol. Oceanogr.*, **50**(2), 727–732.
- Walker, K.T., Nyblade, A.A., Klemperer, S.L., Bokelmann, G.H.R. & Owens, T.J., 2004. On the relationship between extension and anisotropy:

- constraints from shear wave splitting across the East African Plateau, *J. geophys. Res.*, **109**, B08302, doi:10.1029/2003JB002866.
- Webb, S.C., 1998. Broadband seismology and noise under the ocean, *Rev. Geophys.*, **36**, 105–142.
- Webb, S.C. & Crawford, W.C., 1999. Long-period seafloor seismology and deformation under ocean waves, *Bull. seism. Soc. Am.*, **89**, 1535–1542.
- Webb, S.C. & Crawford, W.C., 2010. Shallow-water broadband OBS seismology, *Bull. seism. Soc. Am.*, **100**, 1770–1778.
- Weeraratne, D.S., Forsyth, D.W., Fischer, K.M. & Nyblade, A.A., 2003. Evidence for an upper mantle plume beneath the Tanzanian craton from Rayleigh wave tomography, *J. geophys. Res.*, **108**(B9), 2427, doi:10.1029/2002JB002273.
- Whitmarsh, R.B., Dean, S.M., Minshull, T.A. & Tompkins, M., 2000. Tectonic implications of exposure of lower continental crust beneath the Iberia Abyssal Plain, Northeast Atlantic Ocean: geophysical evidence, *Tectonics*, **19**, 919–942.
- Wopfner, H., 1994. The Malagasy Rift, a chasm in the Tethyan margin of Gondwana, *J. South Asian Earth*, **9**, 451–461.
- Wopfner, H., 2002. Tectonic and climatic events controlling deposition in Tanzanian Karoo basins, *J. Afr. Earth Sci.*, **34**, 167–177.
- Zha, Y., Webb, S.C. & Menke, W., 2013. Determining the orientations of ocean bottom seismometers using ambient noise correlation, *Geophys. Res. Lett.*, **40**(14), 3585–3590.

## SUPPORTING INFORMATION

Supplementary data are available at [GJIRAS](#) online.

**Figure S1.** Estimates of standard deviation of the mean of phase-velocity measurements calculated via Helmholtz tomography. Indi-

vidual event phase-velocity maps are stacked to estimate structural phase velocity which allows for the straightforward estimate of standard deviation. The period of interest is shown in the top right of each panel. All colour scales range from 0 to 0.1. Grey contours indicate regional elevation.

**Figure S2.** Maps of the number of interstation ray paths for a given cell at the periods of interest used when determining teleseismic phase velocity. The colour scale is constant across all periods.

**Figure S3.** Results of a checkboard test of the ambient noise tomography at all periods used in this study. Checkerboard squares are  $0.6^\circ \times 0.6^\circ$ . The top left panel shows the input grids and the resulting grids are shown in the remaining panels. The period of observation is given in the top right-hand corner of each panel. Colour bars give the input/output phase velocity.

**Figure S4.** Maps of the number of crossing interstation ray paths used in the determination of ambient-noise phase velocity. The colour scale is constant across all periods.

**Figure S5.** (a) Phase velocity measured from ambient noise Rayleigh waves at 20 s. (b) Phase velocity measured from teleseismic Rayleigh waves at 20 s.

Please note: Oxford University Press is not responsible for the content or functionality of any supporting materials supplied by the authors. Any queries (other than missing material) should be directed to the corresponding author for the paper.